



HAL
open science

UHBR OPEN-TEST CASE FAN ECL5/CATANA: NON-LINEAR ANALYSIS OF NON-SYNCHRONOUS BLADE VIBRATION AT PART-SPEED CONDITIONS

Anne-Lise Fiquet, Xavier Ottavy, Christoph Brandstetter

► **To cite this version:**

Anne-Lise Fiquet, Xavier Ottavy, Christoph Brandstetter. UHBR OPEN-TEST CASE FAN ECL5/CATANA: NON-LINEAR ANALYSIS OF NON-SYNCHRONOUS BLADE VIBRATION AT PART-SPEED CONDITIONS. 2022. hal-03800486v1

HAL Id: hal-03800486

<https://hal.science/hal-03800486v1>

Preprint submitted on 6 Oct 2022 (v1), last revised 27 Nov 2023 (v2)

HAL is a multi-disciplinary open access archive for the deposit and dissemination of scientific research documents, whether they are published or not. The documents may come from teaching and research institutions in France or abroad, or from public or private research centers.

L'archive ouverte pluridisciplinaire **HAL**, est destinée au dépôt et à la diffusion de documents scientifiques de niveau recherche, publiés ou non, émanant des établissements d'enseignement et de recherche français ou étrangers, des laboratoires publics ou privés.

UHBR OPEN-TEST CASE FAN ECL5/CATANA: NON-LINEAR ANALYSIS OF NON-ASYNCRONOUS BLADE VIBRATION AT PART-SPEED CONDITIONS

Anne-Lise Fiquet

Univ. Lyon, École Centrale de Lyon,
CNRS, Univ. Claude Bernard Lyon 1,
INSA Lyon, LMFA, UMR5509,
69130, Écully, France

Xavier Ottavy

Univ. Lyon, École Centrale de Lyon,
CNRS, Univ. Claude Bernard Lyon 1,
INSA Lyon, LMFA, UMR5509,
69130, Écully, France

Christoph Brandstetter[†]

Univ. Lyon, École Centrale de Lyon,
CNRS, Univ. Claude Bernard Lyon 1,
INSA Lyon, LMFA, UMR5509,
69130, Écully, France
christoph.brandstetter@ec-lyon.fr

ABSTRACT

The onset of non-synchronous-vibrations have been predicted for a composite open-test-case UHBR fan geometry by time-linearized simulations at part-speed conditions. In the current study, time-accurate simulations with harmonic blade oscillations have been conducted to investigate the non-linear behaviour. Results for different operating conditions show the evolution of aeroelastic stability. The lock-in of convected aerodynamic disturbances with structural vibration is analysed for different vibration amplitudes and frequencies. The simulations show the development of multiple wave-numbers, mode scattering and a non-linear dependency on vibration amplitude. The results indicate the possibility of limit-cycle prediction and the necessity of strongly-coupled methods for the assessment of NSV.

Keywords: Fan, Aeroelasticity, Non-Synchronous Vibration

INTRODUCTION

Over the past decades, Non-Synchronous Vibration (NSV) received much attention since it induces dangerous aeroelastic problems in modern high-speed compressor and novel low-speed fans. The term NSV has been widely used to identify aeroelastic phenomena where the characteristic frequency is not related to the shaft frequency without a precise terminology. Numerous phenomena can lead to non-synchronous blade vibrations in

turbomachines, such as flutter [1, 2], buffeting [3] or rotating-stall [4, 5]. According to recent studies [6, 7] a characterization can be derived to describe mechanisms behind vibrations caused by convective phenomena. This type of NSV is driven by small-scale aerodynamic disturbances in form of radial vortices which are convected around the circumference. It has been observed that these aerodynamic disturbances were already present with a characteristic circumferential phase velocity before the onset of blade vibrations [7]. The blockage zone in the tip region caused by the tip leakage flow occurring at off-design conditions is an important factor for unattenuated convection. The disturbances adapt their phase velocity to coincide with a coherent blade eigenmode leading to severe blade vibrations (lock-in). For modern lightweight architectures, aeroelastic interaction mechanisms with complex flow structures are of interest since carbon-fiber composite blades are more flexible and prone to vibration under unsteady aerodynamic excitations. It has been observed that critical operating conditions can occur before the onset of rotating stall, limiting the operating range. Numerous experimental cases have been reported in high-speed compressors [8, 9, 7] and low-speed fans [10] in which convective-NSV phenomena were measured at highly loaded operating conditions with blade vibrations of large amplitude. The numerical prediction of such phenomena is challenging for state-of-the-art methods due to the interdependency between complex flow structures and structure dynamics. However, several cases in literature report prediction of NSV using partial domain simulations [11] or time-linearized methods [12], but indicated the necessity of full-annulus time-accurate simulations such as used for the present study.

The turbomachinery department of Ecole Centrale de Lyon has designed an open-test case of a UHBR fan stage which is

accepted manuscript: Fiquet, A.L., Ottavy, X. and Brandstetter, C. "UHBR open-test-case fan ECL5/CATANA: Non-linear analysis of Non-Synchronous Blade Vibration at part-speed conditions." ISUAAAT-16, Toledo, Spain. September 19 – 23, 2022

[†] address all correspondence to this author

representative of modern low-speed fans. The rotor blades are currently fabricated from layered carbon fiber composites and will be experimentally tested within the European CleanSky-2 project CATANA (Composite Aeroelastics and Aeroacoustics, catana.ec-lyon.fr) in 2022. Coupled fluid-structure phenomena will be experimentally and numerically investigated to provide a comprehensive open dataset for aeroelastic and aeroacoustic research. Previous papers [13, 12] present the design approach, geometry, aerodynamic performance and aeroelastic stability based on RANS and LRANS simulations.

For this configuration, a time-linearized study of aeroelastic stability [14] identified a critical condition at 80% of design speed related to a convective phenomenon in the tip region. Aerodynamic disturbances close to the fan leading edge have been observed to resonate with the second blade eigenmode in nodal diameter ND+5 at a structural eigenfrequency of $f_{vib} = 4.39EO$. The coherent corresponding aerodynamic wave number is $|N_a| = 11$ (aliased on a 16 bladed rotor). Thus, the aerodynamic disturbances propagate with a constant speed of $|\Omega_a^{rel} / \Omega_{rot}| = f_{vib} / |N_a| = 4.39EO / 11 = 0.39$.

To further assess this critical phenomenon, the establishment of aerodynamic disturbances and its possible interaction with the structure is investigated at part-speed conditions with non-linear and time-accurate numerical methods in the present study.

Full-annulus URANS simulations at significant distance from the last numerically stable RANS condition show the emergence of small-scale disturbances convected around the circumference in the tip region near the leading edge [15]. To study the possible interaction between the occurring aerodynamic disturbances and a coherent structural blade eigenmode leading to NSV, fluid-structure interaction (FSI) simulations have been performed. Based on these results, the aeroelastic stability of the fan is investigated in detail. The paper presents a detailed aerodynamic and aeroelastic analysis at different throttle conditions.

A discussion is presented in this paper, including:

- the characterization of aerodynamic instabilities at part-speed conditions based on uncoupled unsteady results
- an analysis of the aeroelastic stability of the fan at off-design conditions for different vibration patterns
- a sensitivity analysis with the prediction of the aeroelastic stability: variation of the vibration amplitude and of the imposed blade eigenfrequency

NUMERICAL SET-UP

The experimental fan stage is composed of 16 composite rotor blades and 31 outlet guide vanes (OGV). The computational domain for unsteady simulation considers the spherical air intake, the fan and a downstream annulus with a choked nozzle to facilitate convergence at highly loaded operating conditions [10],

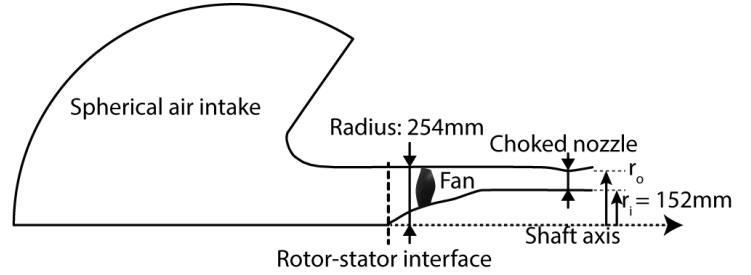


FIGURE 1: FULL-ANNULUS COMPUTATIONAL DOMAIN INCLUDING INLET, INTAKE, FAN AND CONVERGENT/DIVERGENT NOZZLE.

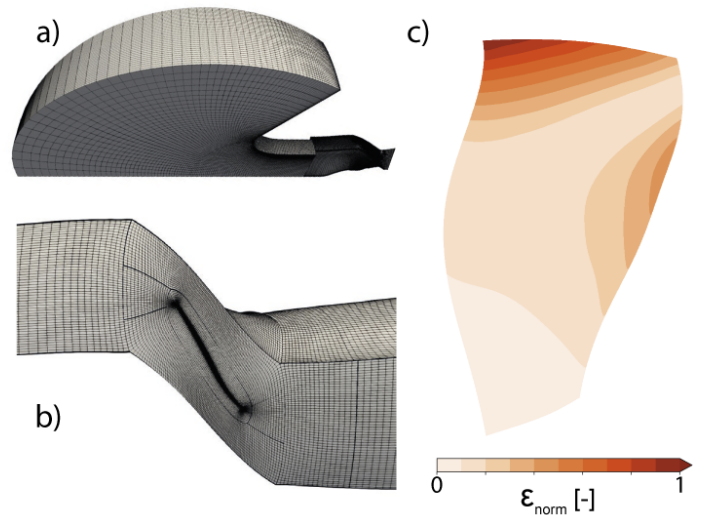


FIGURE 2: DETAILED VISUALIZATION OF STRUCTURED MESH FOR (a) INTAKE, (b) BLADE TO BLADE SECTION AND (c) NORMALIZED MODAL DISPLACEMENT AMPLITUDE OF MODE-2.

as shown in Figure 1. The rotational speed is 80% of design speed (8800 rpm), the corresponding tip clearance 0.87mm at the leading edge and 1.12mm at the trailing edge. Based on negligible influence in pre-studies, the OGV is not modeled in the presented simulations.

A structured mesh has been created using AutoGrid5, as shown in Figure 2 including the spherical air intake (a) and a blade-to-blade view at the fan section (b). The full-annulus domain is modeled with a total number of 34×10^6 nodes with $y^+ \approx 1$. Both unsteady aerodynamic and fluid-structure interaction simulations are performed with elsA, an unsteady Reynolds-Average Navier-Stokes solver, developed by ONERA [16]. The turbulence is modeled with the $k - \omega$ Kok model. Unsteady sim-

OP	Nozzle %	r_o [mm]	\dot{m}_{std} [kg/s]
OP-1	66	174.6	26.00
OP-2	65	171.9	25.59
OP-3	64	169.3	25.09

TABLE 1: NOZZLE CONDITIONS FOR OP-1, OP-2 AND OP-3.

ulations with blade vibration are performed using a dual-time stepping with 20 sub-iterations and 252 physical time steps per period of vibration. The inlet and the air intake are defined in the stationary frame of reference; thus this interface is modeled with a mixing-plane in steady simulations. A sliding-mesh interface is used for unsteady simulations. Full-annulus unsteady simulations without blade vibration start from a steady converged field. After reaching periodic convergence, the unsteady solution is used to initialize the full-annulus simulation with harmonic blade vibration. The involved mode shape corresponds to the second blade eigenmode with a modal frequency of $f_{vib} = 4.5EO$ in the relative frame of reference at 80% of speed. Figure 2c) shows the normalized displacement amplitude of the imposed blade deformation used in the presented FSI simulations. A pronounced torsional component at the blade tip known to be critical for NSV phenomena [17, 18] is observed. Unsteady full-annulus simulations are distributed over 192 processors and at least 10 fan rotations were needed to reach periodic convergence. FSI calculations were running at least for 60 periods of blade vibration to ensure periodic convergence.

STEADY RESULTS

Fan map

Figure 3 presents the fan-only total pressure ratio and isentropic efficiency at part-speed conditions based on single-passage steady calculations. Average performance from converged unsteady full-annulus simulations is depicted as hollow symbols.

The characteristics present a general trend which is representative of modern UHBR fans detailed in the literature. Three operating points denoted as OP-1, OP-2 and OP-3 will be investigated in this paper, and the corresponding nozzle conditions are presented in Table 1 where r_o represents the outer radius of the choked nozzle (see Figure 1). Both steady and unsteady simulations predict an equivalent total pressure ratio and isentropic efficiency at OP-1 with a massflow rate of $\dot{m} = 26.0$ kg/s. For OP-2 and OP-3 where stronger aerodynamic disturbances are observed, a moderate increase of total pressure ratio is observed compared to RANS prediction.

Flow structures

Comparison of the flow field between RANS results and the time-average URANS simulation at highly loaded conditions (OP-3) is illustrated in Figure 4 by plotting the blade-to-blade view at 95% of channel height contoured by the relative Mach

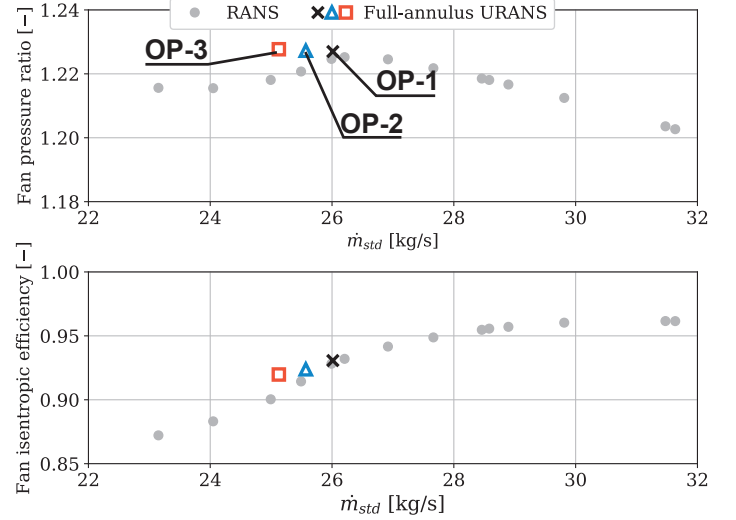


FIGURE 3: MASS-AVERAGED FAN CHARACTERISTICS AT 80% OF THE DESIGN SPEED FROM STEADY AND UNSTEADY SIMULATIONS: FAN-ONLY TOTAL PRESSURE RATIO AND ISENTROPIC EFFICIENCY.

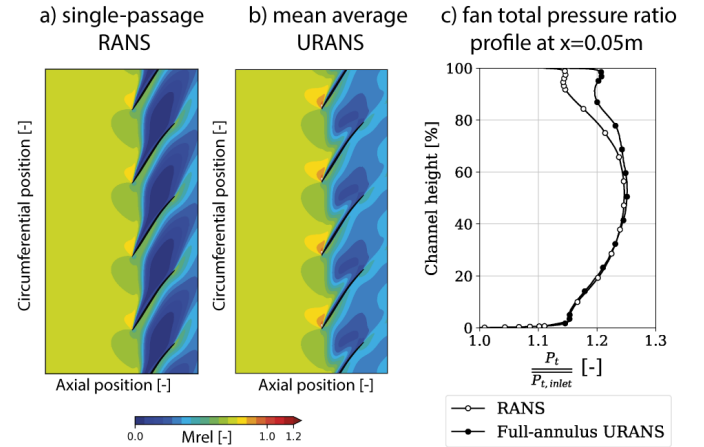
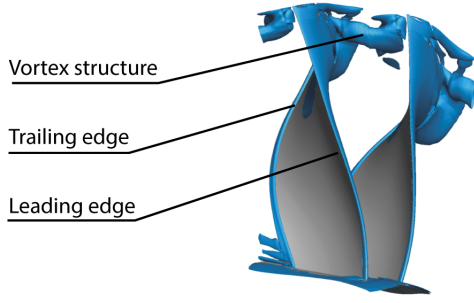


FIGURE 4: CONTOURS AT 95%H OF RELATIVE MACH NUMBER FROM RANS SIMULATION (a) AND TIME-AVERAGE URANS SIMULATION (b) AND FAN TOTAL PRESSURE RATIO PROFILE AT $x = 0.05m$ DOWNSTREAM OF THE FAN (c) FOR OP-3.

a) Q-criterion visualization



b) B2B view at 95%H

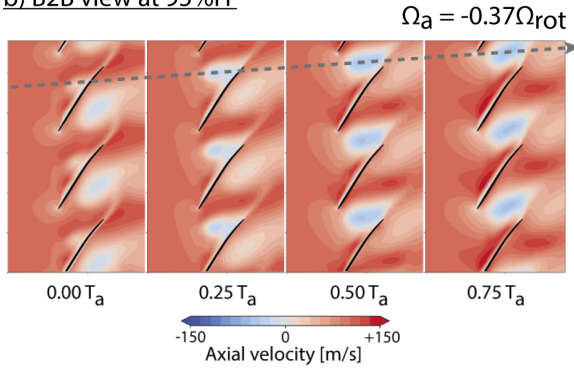


FIGURE 5: AERODYNAMIC DISTURBANCES NEAR OP-3 AT 80% OF DESIGN SPEED: (a) SNAPSHOT OF VORTEX STRUCTURES, ISOCONTOUR AT Q-CRITERION= $2 \cdot 10^7$, VALUES BLANKED ABOVE 99% H AND (b) TEMPORAL EVOLUTION OF A BLADE-TO-BLADE VIEW AT 95% H CONTOURED BY AXIAL VELOCITY [15].

number (a, b) and the time average radial profile of the converged unsteady solution compared to the RANS simulation (c). For this operating condition, the rotor is running subsonic. A large blockage zone is observed in the inter-blade passage and its topology differs between RANS and URANS predictions. The single-passage steady result predicts a larger blockage zone compared to the time average unsteady simulation which leads to a drop in total pressure ratio and isentropic efficiency as observed in Figure 3. It can be seen with the radial profile that the fan total pressure ratio predicted by RANS simulation is reduced in the tip region, from 60% H up to the casing. A detailed discussion on the difference between RANS and URANS simulations for this configuration is provided in [15].

UNSTEADY UNCOUPLED RESULTS

In [15], unsteady full-annulus simulation near OP-3 develops small-scale disturbances in form radial vortices. Figure 5 a) illustrates the isocontour of the Q-criterion at one time instant to emphasize the vortex structures observed in the inter-blade

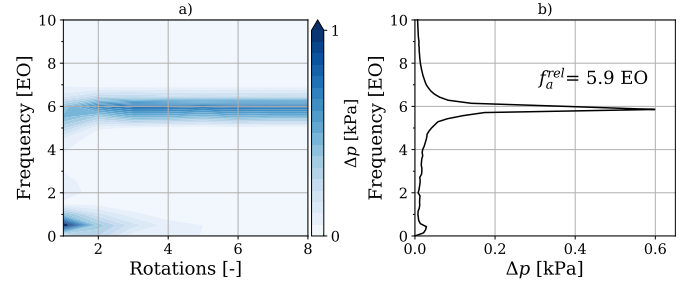


FIGURE 6: SPECTRUM ANALYSIS OF PRESSURE FLUCTUATIONS IN THE ROTATING FRAME OF REFERENCE MEASURED AT 80% H NEAR THE LEADING EDGE AT OP-3: (a) FREQUENCY SPECTROGRAM DURING THE TRANSIENT SIMULATION AND (b) FREQUENCY SPECTRUM AVERAGED OVER THE LAST 7 CONVERGED ROTATIONS.

passage. A vortex develops on the suction side and propagates towards the pressure side of the adjacent blade in the circumferential direction with a speed of $-0.37\Omega_{rot}$. The propagation is illustrated in the blade-to-blade view of the axial velocity at 95% of channel height during one period of disturbance T_a in Fig. 5 b). Since all blades are identical in the full-annulus simulation, the aerodynamic wave number N_a induced by the occurring aerodynamic disturbances is equal to the blade count $N_a = -N_b = -16$.

Spectral analysis is performed based on pressure fluctuations at 80% H near the leading edge in the rotating frame of reference at OP-3. and presented in Figure 6. The unsteady simulation converged rapidly towards a periodic solution after 2 simulated rotations, depicted in the spectrogram (a). The frequency related to the occurring small-scale disturbances in the rotating frame of reference is $f_a^{rel} = 5.9EO$ corresponding to a circumferential propagating speed of $\Omega_a^{rel}/\Omega_{rot} = f_a^{rel}/N_a = -0.37$.

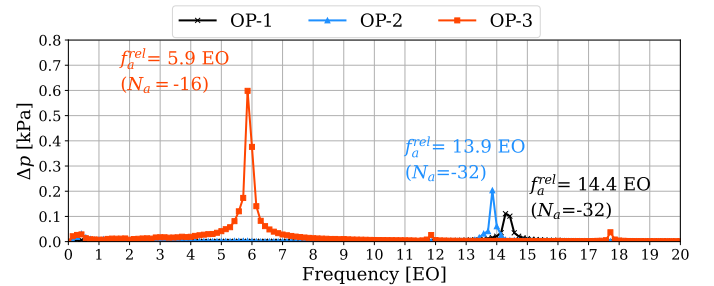


FIGURE 7: FREQUENCY SPECTRA OF PRESSURE FLUCTUATIONS IN THE ROTATING FRAME OF REFERENCE AT 80% H NEAR THE LEADING-EDGE COMPUTED WITH THE LAST 7 CONVERGED ROTATIONS FOR OP-1, OP-2 AND OP-3.

OP	$f_a^{rel} [EO]$	$N_a [-]$	$\Omega_a^{rel} / \Omega_{rot} [-]$	ND _{critical}
OP-1	14.4	-32	-0.45	+6
OP-2	13.9	-32	-0.43	+6/+5
OP-3	5.9	-16	-0.37	+4

TABLE 2: AERODYNAMIC DISTURBANCES CHARACTERISTICS.

Comparable small-scale disturbances have been observed at higher masflow rates for OP1 and OP2 (see Figure 3), but with slightly different characteristics as shown by frequency spectra presented in Figure 7. Clear peaks corresponding to the aerodynamic disturbances in the tip region from OP-1 towards OP-3 are observed at $f_a^{rel} = 14.4EO$, $f_a^{rel} = 13.9EO$ and $f_a^{rel} = 5.9EO$ respectively. The amplitude associated to the occurring aerodynamic disturbances grows with the reduction of the massflow rate.

Spatial Fourier transform indicates, that for OP-1 and OP-2 the dominant aerodynamic wave number is $|N_a| = 32$ (2 times the blade count $N_b = 16$), whereas at OP-3 the dominant mode is $|N_a| = 16$. The associated $\Omega_a^{rel} / \Omega_{rot}$ shows a significant reduction of the relative disturbance propagation speed from -45% at OP-1 to -37% at OP-3, but all values indicate convective phenomena. Using these values, the most critical nodal diameter susceptible for NSV can be derived according to [11]. With a structural blade eigenfrequency of $f_{vib} = 4.5EO$ the critical nodal diameter at OP-3 is calculated as follows: $N_a = f_{vib} / (\Omega_a^{rel} / \Omega_{rot}) = 4.5 / (-0.37) \approx -12$ which corresponds to the development of nodal diameter ND+4. For all simulated operating conditions, the critical values are presented in Table 2.

COUPLED UNSTEADY RESULTS

Numerical aeroelastic analysis is performed by computing the harmonic pressure fluctuation on the blade surface to derive work per cycle of vibration W . Per convention, negative work entry ($W < 0$) represents a net transfer into the structure, indicating unstable behaviour, positive work ($W > 0$) implies stable conditions. The aerodynamic damping is derived by Equation 1 with the modal kinetic energy U , the modal mass M_{vib} , the vibration amplitude a_{vib} and the angular vibration frequency $\omega_{vib} = 2\pi f_{vib}$.

$$\xi_{aero} = \frac{W}{U} = \frac{W}{2\pi M_{vib} a_{vib}^2 \omega_{vib}^2} \quad (1)$$

According to the theoretically critical conditions in Table 2, coupled simulations have been conducted for all three operating conditions and a vibration amplitude of $a_{vib} = 0.25mm$ ($\approx 0.52\%$ of the axial chord at the tip). Figure 8 presents the transient aerodynamic damping of Mode-2/ND+4 for OP-1, OP-2 and OP-3.

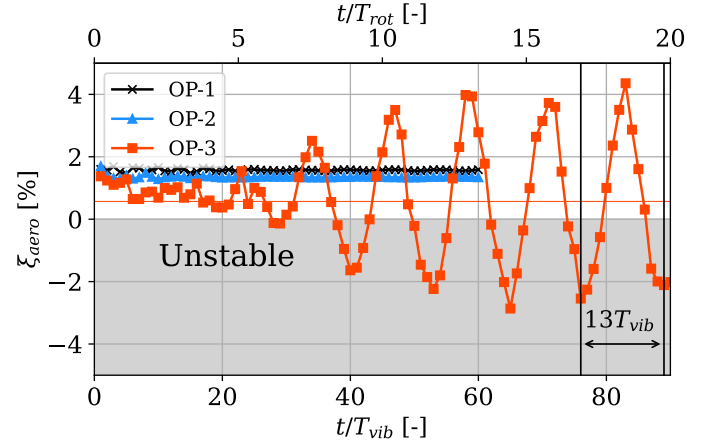


FIGURE 8: TRANSIENT AERODYNAMIC DAMPING FROM FSI SIMULATIONS WITH HARMONIC BLADE VIBRATION IMPOSED ON MODE-2/ND+4 FOR OP-1, OP-2 AND OP-3.

It can be observed that the aerodynamic damping converged rapidly at OP-1 and OP-2 towards a positive value with small variations after 20 periods of blade vibration. At OP-3, FSI simulation reached periodic convergence after approximately 50 periods of blade vibration with strong fluctuations of the aerodynamic damping. The time average value based on results after $30T_{vib}$ is depicted in this figure by the orange line and a beating with a period of $13T_{vib} \approx 2.9T_{rot}$ is observed (orange curve with square symbols). The beating will be discussed in the Sensitivity Analysis section.

In Figure 9, the aerodynamic damping variations of Mode-2 as function of nodal diameter of all operating conditions is plotted. A average aerodynamic damping is computed using results after 30 periods of blade vibration. For OP-1 and OP-2, it evolves smoothly. A critical operating condition is observed at OP-3 with Mode-2/ND+4 since the average aerodynamic damping is marginally positive with variations of $\pm 3.61\%$, indicating intermittent unstable conditions as observed in Figure 8. Table 3 summarizes the average aerodynamic damping for all operating conditions. For OP-1 and OP-2, FSI simulations predict continuously stable operating conditions. Critical behaviour is observed for OP-3 with Mode-2/ND+4.

Frequency spectra of pressure fluctuations at 80% of channel height near the leading edge from URANS results (dotted curves) and FSI simulation with blade oscillations on Mode-2/ND+4 (continued curve) are shown in Figure 10 for all operating points. A clear peak at $f_{vib} = 4.5EO$ with an aerodynamic wave number of $N_a = -12$ (ND+4 aliased on a 16 bladed rotor) is observed, corresponding to the structural eigenfrequency of Mode-2. For OP-1, a shift in frequency of the aerodynamic disturbances

Time average aerodynamic damping $\overline{\xi}_{aero}$ [%]				
OP	Mode-2			
	ND+3	ND+4	ND+5	ND+6
OP-1	-	1.57(± 0.02)	1.67(± 0.02)	1.82(± 0.02)
OP-2	2.02(± 0.02)	1.35(± 0.01)	1.67(± 0.02)	1.82(± 0.02)
OP-3	4.49(± 0.69)	0.57 (± 3.61)	1.29(± 0.47)	-

TABLE 3: AVERAGE AERODAMPING AFTER 30 PERIODS OF BLADE VIBRATION.

$N_a = -32$ from $14.4EO$ to $14.1EO$ is observed between URANS and FSI simulations. For OP-2, the frequency of aerodynamic disturbances is comparable between both simulations. At OP-3 numerous aerodynamic wave numbers develop into the simulation, associated to different frequency peaks as indicated in Figure 8, derived by spatial Fourier transformation. Wave number $N_a = -16$ is still present in the FSI simulation with a slightly shifted frequency of $f_a^{rel} = 5.8EO$. The modulation of the nodal diameter with the blade count $|N_{a,mod+}| = N_b + ND = 16 + 4$ yielding to $|N_{a,mod+}| = 20$ is also visible in the frequency spectra at $f^{rel} = 7.4EO$, indicating non-linear scattering.

At OP-3, an intermittently unstable behaviour is predicted by FSI simulation for Mode-2/ND+4 in contrast to Mode-2/ND+3 which remains highly stable as shown in Figure 11. This figure represents the transient aerodynamic damping for both nodal diameters ND+3 and ND+4.

Comparable to the results for ND+4 in Figure 10, the fre-

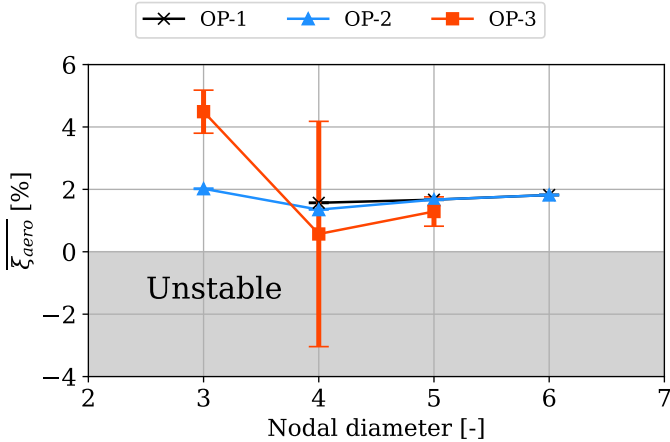


FIGURE 9: AVERAGE AERODYNAMIC DAMPING AND FLUCTUATIONS AS A FUNCTION OF NODAL DIAMETER FOR OP-1, OP-2 AND OP-3.

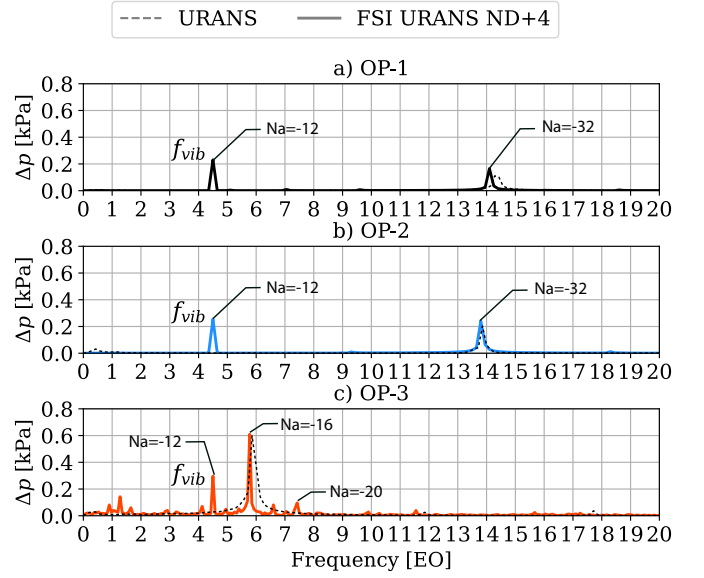


FIGURE 10: FREQUENCY SPECTRA OF PRESSURE FLUCTUATIONS IN THE ROTATING FRAME OF REFERENCE AT 80% H NEAR THE LEADING EDGE FROM FSI SIMULATIONS WITH BLADE OSCILLATIONS ON **MODE-2/ND+4** FOR OP-1 (a), OP-2 (b) AND OP-3 (c) COMPUTED WITH THE LAST 30 CONVERGED PERIODS OF BLADE VIBRATION.

quency spectrum of unsteady pressure at 80% H near the leading edge in the rotating frame of reference plotted in Figure 12 indicates the presence of numerous wave numbers for ND+3. Compared to the URANS simulation a reduction of $N_a = -16$ content is observed with a slight shift in frequency. The amplitude corresponding to the blade eigenfrequency $f_{vib} = 4.5EO$ is even higher than for the ND+4 case (compare Figure 10c). This point is interesting, as obviously coherent lock-in of aerodynamic disturbances with Mode-2/ND+3 is possible, but the associated aerodynamic damping is positive. At ND+4, the coupled simulation contains significant frequency content which is not locked with the blade vibration ($N_a = -16$), but intermittent unstable conditions occur due to the development of wave number $N_a = -12$.

In order to quantify the lock-in of propagation speed, Table 4 summarizes the derived values. For the stable case ND+3, the locked propagation speed of $N_a = -13$ is $-34.6\% \Omega_{rot}$, representing a significant shift compared to the free propagation speed of $-37\% \Omega_{rot}$ (Table 2). For unstable ND+4, the corresponding wave number $N_a = -12$ propagates with only a slight shift to $-37.5\% \Omega_{rot}$.

To analyze the cause for negative aerodynamic damping at ND+4 further, the mean local work at the blade surface of

Mode-2/ND+3			Mode-2/ND+4		
Stable			Periodically Unstable		
N_a [-]	f_a^{rel} [EO]	$\frac{\Omega_a^{rel}}{\Omega_{rot}}$ [-]	N_a [-]	f_a^{rel} [EO]	$\frac{\Omega_a^{rel}}{\Omega_{rot}}$ [-]
-13	4.5	-0.346	-12	4.5	-0.375
-16	5.9	-0.369	-16	5.8	-0.3625
-19	7.2	-0.379	-20	7.4	-0.37

TABLE 4: AERODYNAMIC WAVE CHARACTERISTICS AT OP-3 FROM FSI SIMULATIONS.

all blades derived by Equation 1 is plotted Figure 13 for three relevant cycles of vibration indicated in Figure 11 (black circles). Since the fan is predicted stable for Mode-2/ND+3 at OP-3, results from the last cycle of vibration is used as reference. For Mode-2/ND+4, two different cycles are considered: one at $t = 86T_{vib}$ which is marginally stable and the last unstable cycle at $t = 90T_{vib}$. The local work is considered stabilizing for positive values (blue) and destabilizing for negative values (red). The work is concentrated at the tip of the blade (compare mode shape in Figure 2c). At ND+3, both pressure side and suction side are equivalently involved in overall stability. On the suction side, a large stabilizing zone is observed from the leading edge to mid-chord, in contrast with the blade trailing-edge which is destabilizing. On the pressure side, close to the leading edge, the local work is positive inducing a stabilizing zone. Integration of this local work indicates a stable cycle.

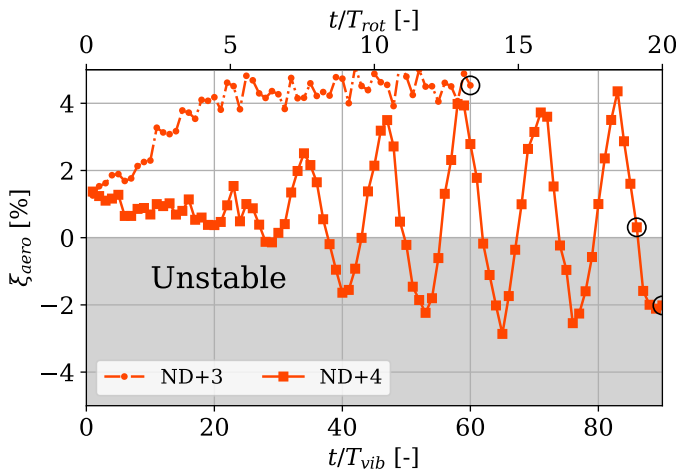


FIGURE 11: TRANSIENT AERODYNAMIC DAMPING FROM FSI SIMULATIONS WITH HARMONIC BLADE VIBRATION IMPOSED ON MODE-2/ND+3 AND MODE-2/ND+4 FOR OP-1, OP-2 AND OP-3.

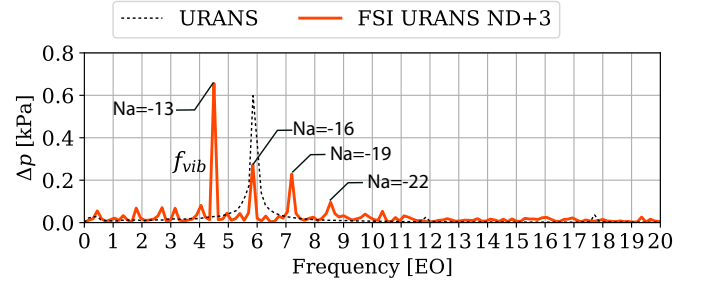


FIGURE 12: FREQUENCY SPECTRUM OF PRESSURE FLUCTUATIONS IN THE ROTATING FRAME OF REFERENCE AT 80%H NEAR THE LEADING EDGE FROM FSI SIMULATIONS WITH BLADE OSCILLATIONS ON MODE-2/ND+3 FOR OP-3.

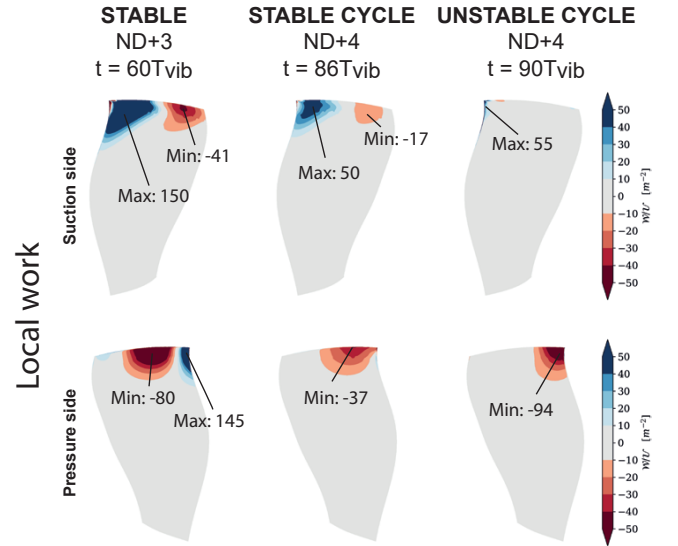


FIGURE 13: LOCAL WORK AND UNSTEADY PRESSURE AT OP-3 FOR MODE-2/ND+3, AMPLITUDE 0.25mm AT $t = 60t_{vib}$, MODE-2/ND+4 AT STABLE CYCLE $t = 86t_{vib}$ AND MODE-2/ND+4 AT UNSTABLE CYCLE $t = 90t_{vib}$ (SEE FIGURE 11).

At ND+4 for the stable cycle of vibration, the amplitude of the local work is reduced. On the suction side, the topology of local work is comparable with Mode-2/ND+3. The negative zone of local work on the pressure side is located further upstream and the positive zone near the leading edge is strongly reduced compared to Mode-2/ND+3. For the unstable cycle of vibration, the pattern on the suction side differs significantly. Only a negative zone of local work is located near the leading edge. For this condition, the simulation does not converge periodically with the

blade vibration but still contains a significant beating amplitude, resulting in a topological fluctuation of the work density, which is not a numerical error.

The topology of the unsteady pressure distribution is comparable between the stable cycle at ND+4 and ND+3 and changes merely for the unstable cycle. Here, strong fluctuations are observed at the leading edge on the pressure side.

To visualize the unsteady flow field in the coupled simulations, Figure 14 shows snapshots of entropy fluctuations at 95% of channel height, depicting the separation of vortical structures near the leading edge, which propagate in the circumferential direction. This representation corresponds well with previous studies on NSV [10, 15].

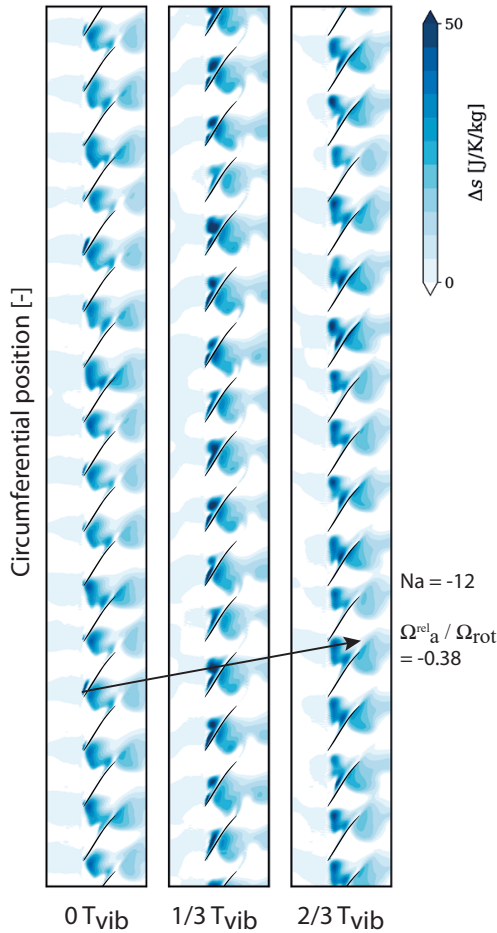


FIGURE 14: TEMPORAL EVOLUTION OF A BLADE TO BLADE VIEW AT 95%*H* CONTOURED BY ENTROPY FLUCTUATIONS AT OP-3 WITH BLADE OSCILLATION ON MODE-2/ND+4 AT 80% OF DESIGN SPEED: LOCK-IN BETWEEN SMALL-SCALE DISTURBANCES AND STRUCTURAL VIBRATION PATTERN.

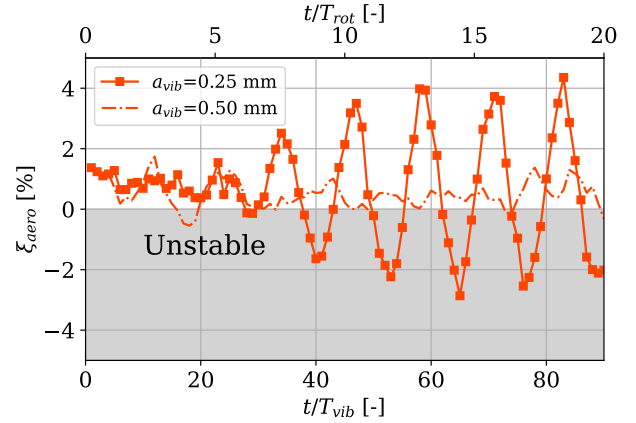


FIGURE 15: TRANSIENT AERODYNAMIC DAMPING FROM FSI SIMULATION WITH BLADE OSCILLATION IMPOSED ON MODE-2/ND+4 WITH MAXIMAL AMPLITUDE OF $a_{vib} = 0.25mm$ AND $a_{vib} = 0.50mm$ AT OP-3.

SENSITIVITY ANALYSIS AND DISCUSSION

Amplitude variation

To analyze saturation effects, the vibration amplitude has been increased by 100% to a maximum deflection of $a_{vib} = 0.5mm$ at the leading edge. Results for the temporal evolution of aerodynamic damping are presented in Figure 15.

Instead of the beating behaviour with alternating stable and unstable periods observed for vibration amplitude $a_{vib} = 0.25mm$, the increased motion leads to a periodically converged stable behaviour with low fluctuations between 0 and 1% of the aerodynamic damping. This non-linear behaviour is in agreement with experiments [19] of a comparable low-speed fan, which show that limit-cycle oscillations of the order of the blade thickness establish at stable aerodynamic conditions before the onset of rotating stall. With increased throttling, vibration amplitude and associated unsteady pressure signatures increase continuously. The presented results indicate, that marginally stable behaviour will be achieved at OP-3 for vibration amplitudes between 0.25mm and 0.50mm, which can be quantified in planned experiments. It is possible, that such a variation of blade vibration amplitudes in time-accurate simulation provides a possibility to predict Limit-Cycle-Oscillations and incorporate saturation effects in reduced order models for Non-Synchronous-Vibration. This provides a significant step forward compared to pure stability analysis such as presented in [6]. These observations show that the prediction of the fan stability is strongly affected by non-linear mechanisms.

In Figure 16, the frequency spectrum of unsteady pressure for Mode-2/ND+4 with $a_{vib} = 0.50mm$ shows comparable results to Mode-2/ND+3 where the fan presents a stable behaviour (see Figure 12). A significant increase in amplitude is observed for

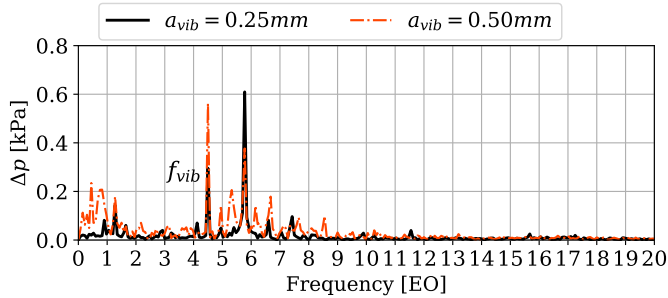


FIGURE 16: FREQUENCY SPECTRA OF PRESSURE FLUCTUATIONS IN THE ROTATING FRAME OF REFERENCE AT 80%*H* NEAR THE LEADING EDGE FROM FSI SIMULATIONS WITH BLADE OSCILLATIONS ON MODE-2/ND+4 WITH $a_{vib} = 0.25mm$ AND $a_{vib} = 0.50mm$ AT OP-3.

f_{vib} . Intensity of the higher wave number disturbances observed for $a_{vib} = 0.25mm$ is reduced and distributed in a broad band of the spectrum.

Frequency variation

The study presented in [6] has shown a significant influence of the disturbance propagation speed on aerodynamic damping. This was related to the ratio between the blade vibration frequency and the phase velocity of aerodynamic disturbances. As the latter is dependent of the aerodynamic field and cannot be varied in the simulation, the sensitivity of the results towards blade oscillation frequency has been varied. A series of simulations with a maximum shift of vibration frequency of $\pm 4\%$ for the reference amplitude of $a_{vib} = 0.25mm$ has shown negligible influence on the time-average aerodynamic damping. However, the periodic convergence was affected as presented in Figure 17. The simulations still show beating amplitudes of aerodynamic damping but the beating frequency is significantly altered. For a vibration frequency of $0.96f_{vib}$, a much longer beating period is observed, while an increased frequency shortens the beating period. These results cannot be directly compared to those presented in [6], because the FSI simulations are weakly coupled. Harmonic blade oscillation is prescribed and enforced throughout the simulation, leading to establishment of multiple wave numbers, scattering and modulations (see Fig. 10 and 12). In the coupled model of [6], the system locks-in to an aeroelastic frequency which is not equal to the vacuum frequency f_{vib} . Hence, to study such influence, strongly-coupled simulations will be necessary in the future. However, the fact that the average value of aerodynamic damping is mostly unaffected by the prescribed frequency and merely the beating frequency and amplitude vary is a clear indicator that the presented simulations are valuable for the prediction of NSV onset and limit cycle amplitudes. The non-linear scattering and beating behaviour must be addressed in

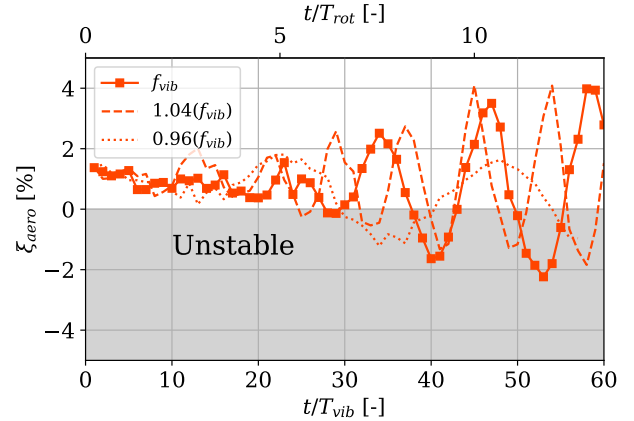


FIGURE 17: TRANSIENT AERODYNAMIC DAMPING FROM FSI SIMULATION WITH BLADE OSCILLATION IMPOSED ON MODE-2/ND+4 AT OP-3 WITH A FREQUENCY VARIATION OF $\pm 4\%$.

future works with strong coupling.

CONCLUSION

Unsteady aeroelastic phenomena at off-design conditions have been numerically studied in the open-test-case fan ECL5 which is representative of modern lightweight UHBR fan architectures. At part-speed condition (80% of design speed), the unsteady (uncoupled) full-annulus simulation develops small-scale disturbances in form of radial vortices at operating conditions far from the last converged steady calculation. For all presented operating conditions, these disturbances travel around the circumference at a circumferential speed between $-45\%\Omega_{rot}$ and $-37\%\Omega_{rot}$ in the rotating frame of reference.

Since this type of disturbances is known to lead to non-synchronous blade vibrations due to lock-in with a structural blade eigenmode, unsteady coupled FSI simulations have been carried out to predict the aeroelastic stability of the fan. Reduction of the massflow rate leads to decreased aeroelastic stability, in agreement with literature. The critical nodal diameters correspond to those predicted by a reduced order model based on uncoupled unsteady simulations. For a specific operating condition, periodically alternating stable and unstable cycles are observed. Increased blade vibration amplitude eliminates the beating behaviour and an average stable aerodynamic damping indicates the possibility of limit-cycle prediction. Beating frequency and scattered mode amplitude were related to the vibration frequency. The behaviour is associated to a non-linear interaction, involving the presence of multiple aerodynamic wave numbers and the overconstrained simulation with pre-imposed harmonic blade vibration. The presented results show significant progress compared to linear stability analysis (NSV onset) and provide ground for limit-cycle prediction, but clearly indicate the neces-

sity of strongly-coupled methods.

NOMENCLATURE

Δp	Pressure fluctuation [Pa]
ΔS	Unsteady specific Entropy [J/(kgK)]
P_m	Amplitude of static pressure [Pa]
M_{rel}	Relative Mach Number [-]
N_a	Aerodynamic wave number [-]
ND	Nodal diameter [-]
N_b	Number of rotor blades [-]
Ω_{rot}	Angular shaft velocity [rad/s]
Ω	Angular velocity [rad/s]
T_{rot}	Rotational period [s]
f_{rot}	Rotational frequency [Hz]
a_{vib}	Vibration amplitude [mm]
T_{vib}	Vibration period [s]
M_{vib}	Modal mass [kg]
f_{vib}	Vibration frequency [Hz]
U	Modal kinetic energy [J]
W	Work [J]
\dot{m}_{std}	Standard massflow rate [kg/s]
ξ_{aero}	Aerodynamic damping [-]
r	Radius [m]
H	Channel height [%]
V_x	Axial velocity [m/s]
NSV	Non-Synchronous Vibrations
OGV	Outlet Guide Vane
OP	Operating point
UHBR	Ultra High Bypass Ratio
\cdot_{rel}	Rotating frame of reference
\cdot_a	Aerodynamic disturbance

ACKNOWLEDGMENT

The authors are grateful for the technical advice and contributions of Benoit Paoletti. This project has received funding from the Clean Sky 2 Joint Undertaking (JU) under grand agreement N°864719. The JU receives support from the European Union’s Horizon 2020 research and innovation program and the Clean Sky 2 JU members other than the Union. This publication reflects only the author’s view and the JU is not responsible for any use that may be made of the information it contains. The development of the Open Test Case rotor fan is supported by CIRT (Consortium Industrie-Recherche en Turbomachine).

REFERENCES

- [1] Vahdati, M., Sayma, A. I., Marshall, J. G., and Imregun, M., 2001. “Mechanisms and Prediction Methods for Fan Blade Stall Flutter”. *Journal of Propulsion and Power*, **17**(5), pp. 1100–1108.
- [2] Corral, R., and Vega, A., 2016. “Physics of Vibrating Turbine Airfoils at Low Reduced Frequency”. *Journal of Propulsion and Power*, **32**(2), pp. 325–336.
- [3] Harris, J., Lad, B., and Stapelfeldt, S., 2020. “Investigating the Causes of Outlet Guide Vane Buffeting”. In Proc. ASME Turbo Expo 2020, pp. GT2020–16063.
- [4] Iim, H., Chen, X.-Y., and Zha, G., 2012. “Detached-Eddy Simulation of Rotating Stall Inception for a Full-Annulus Transonic Rotor”. *J. Propul. Power*, **28**(4), pp. 782–798.
- [5] Kim, S., Pullan, G., Hall, C. A., Grewe, R. P., Wilson, M. J., and Gunn, E., 2019. “Stall Inception in Low-Pressure Ratio Fans”. *J. Turbomach.*, **141**(7), p. 071005.
- [6] Brandstetter, C., and Stapelfeldt, S., 2021. “Analysis of a linear model for non-synchronous vibrations near stall”. *Int. J. Turbomach., Propulsion and Power*, **6**(3), p. 26.
- [7] Brandstetter, C., Juengst, M., and Schiffer, H.-P., 2018. “Measurements of Radial Vortices, Spill Forward, and Vortex Breakdown in a Transonic Compressor”. *J. Turbomach.*, **140**(6), p. 061004.
- [8] Baumgartner, M., Kameier, F., and Hourmouziadis, J., 1995. “Non-engine order blade vibration in a high pressure compressor”. In Proc. 12th ISABE (Int. Society for Air Breathing Engines).
- [9] Kielb, R. E., Barter, J. W., Thomas, J. P., and Hall, K. C., 2003. “Blade Excitation by Aerodynamic Instabilities: A Compressor Blade Study”. In Proc. ASME Turbo Expo 2003, pp. 399–406.
- [10] Rodrigues, M., Soulat, L., Paoletti, B., Ottavy, X., and Brandstetter, C., 2021. “Aerodynamic investigation of a composite low-speed fan for UHBR Application”. *J. Turbomach.*, **143**(10), p. 101004.
- [11] Stapelfeldt, S., and Brandstetter, C., 2020. “Non-synchronous vibration in axial compressors: Lock-in mechanism and semi-analytical model”. *J. Sound and Vibration*, **488**, p. 115649.
- [12] Pages, V., Duquesne, P., Aubert, S., Blanc, L., Ferrand, P., Ottavy, X., and Brandstetter, C., 2022. “UHBR Open-Test-Case Fan ECL5/CATANA”. *Int. J. Turbomach., Propulsion and Power*, **7**(2), p. 17.
- [13] Brandstetter, C., Pages, V., Duquesne, P., Paoletti, B., Aubert, S., and Ottavy, X., 2019. “Project PHARE-2 : A High-Speed UHBR Fan Test Facility for a New Open-Test Case”. *J. Turbomach.*, **141**(10), p. 101004.
- [14] Pages, V., Duquesne, P., Ottavy, X., Ferrand, P., Aubert, S., Blanc, L., and Brandstetter, C., 2021. “UHBR open-test-case fan ECL5/CATANA, Part 2 : Mechanical and aeroelastic stability analysis”. In Proc. ETC14, ETC2021-625.
- [15] Fiquet, A.-L., Ottavy, X., and Brandstetter, C., 2022. “Uhbr Open-Test-Case Fan Ecl5/Catana: Numerical Investigation Near The Stability Limit Including Aerodynamic Mistuning”. In Proc. ASME Turbo Expo 2022, GT2022-77992.
- [16] Cambier, L., Heib, S., and Plot, S., 2013. “The Onera elsA CFD software: input from research and feedback from industry”. *Mechanics and Industry*, **14**(3), pp. 159–174.
- [17] Duquesne, P., Mahieux, B., Aubert, S., and Ferrand, P., 2019. “Sensitivity of the aerodynamics damping coefficient prediction to the turbulence modelling conjugated with the vibration mode shape”. In Proc. 13th European Conference on Turbomachinery Fluid dynamics and Thermodynamics.
- [18] Brandstetter, C., Paoletti, B., and Ottavy, X., 2019. “Compressible Modal Instability Onset in an Aerodynamically Mistuned Transonic Fan”. *J. Turbomach.*, **141**(3), p. 031004.
- [19] Schneider, A., Paoletti, B., Ottavy, X., and Brandstetter, C., 2022. “Influence Of A Turbulence Control Screen On The Aerodynamic And Aeroelastic Behavior Of A Uhbr Fan”. In Proc. ASME Turbo Expo 2022, GT2022-81961.